

# Cosmogenic Backgrounds in Borexino at 3800 m water-equivalent depth

Borexino collaboration

G. Bellini,<sup>a</sup> J. Benziger,<sup>b</sup> D. Bick,<sup>c</sup> G. Bonfini,<sup>d</sup> D. Bravo,<sup>e</sup>  
M. Buizza Avanzini,<sup>a</sup> B. Caccianiga,<sup>a</sup> L. Cadonati,<sup>f</sup> F. Calaprice,<sup>g</sup>  
P. Cavalcante,<sup>d</sup> A. Chavarria,<sup>g</sup> A. Chepurinov,<sup>h</sup> D. D'Angelo,<sup>a</sup>  
S. Davini,<sup>i</sup> A. Derbin,<sup>j</sup> A. Empl,<sup>i</sup> A. Etenko,<sup>k</sup> K. Fomenko,<sup>d,l</sup>  
D. Franco,<sup>m</sup> C. Galbiati,<sup>g</sup> S. Gazzana,<sup>d</sup> C. Ghiano,<sup>m</sup>  
M. Giammarchi,<sup>a</sup> M. Göger-Neff,<sup>o</sup> A. Goretti,<sup>g</sup> L. Grandi,<sup>g</sup>  
C. Hagner,<sup>c</sup> E. Hungerford,<sup>i</sup> Aldo Ianni,<sup>d</sup> Andrea Ianni,<sup>g</sup>  
V. Kobychiev,<sup>p</sup> D. Korablev,<sup>l</sup> G. Korga,<sup>i</sup> D. Kryn,<sup>m</sup>  
M. Laubenstein,<sup>d</sup> T. Lewke,<sup>o</sup> E. Litvinovich,<sup>k</sup> B. Loer,<sup>g</sup>  
P. Lombardi,<sup>a</sup> F. Lombardi,<sup>d</sup> L. Ludhova,<sup>a</sup> G. Lukyanchenko,<sup>k</sup>  
I. Machulin,<sup>k</sup> S. Manecki,<sup>e</sup> W. Maneschg,<sup>n</sup> G. Manuzio,<sup>q</sup>  
Q. Meindl,<sup>o</sup> E. Meroni,<sup>a</sup> L. Miramonti,<sup>a</sup> M. Misiaszek,<sup>r</sup>  
R. Möllenberg,<sup>o</sup> P. Mosteiro,<sup>g</sup> V. Muratova,<sup>j</sup> L. Oberauer,<sup>o</sup>  
M. Obolensky,<sup>m</sup> F. Ortica,<sup>s</sup> K. Otis,<sup>f</sup> M. Pallavicini,<sup>q</sup> L. Papp,<sup>e</sup>  
L. Perasso,<sup>q</sup> S. Perasso,<sup>m</sup> A. Pocar,<sup>f</sup> G. Ranucci,<sup>a</sup> A. Razeto,<sup>d</sup>  
A. Re,<sup>a</sup> A. Romani,<sup>s</sup> N. Rossi,<sup>d</sup> R. Saldanha,<sup>g</sup> C. Salvo,<sup>q</sup>  
S. Schönert,<sup>o</sup> H. Simgen,<sup>n</sup> M. Skorokhvatov,<sup>k</sup> O. Smirnov,<sup>l</sup>  
A. Sotnikov,<sup>l</sup> S. Sukhotin,<sup>k</sup> Y. Suvorov,<sup>t,k</sup> R. Tartaglia,<sup>d</sup>  
G. Testera,<sup>q</sup> D. Vignaud,<sup>m</sup> R.B. Vogelaar,<sup>e</sup> F. von Feilitzsch,<sup>o</sup>  
J. Winter,<sup>o</sup> M. Wojcik,<sup>r</sup> A. Wright,<sup>g</sup> M. Wurm,<sup>c</sup> J. Xu,<sup>g</sup>  
O. Zaimidoroga,<sup>l</sup> S. Zavatarelli,<sup>q</sup> G. Zuzel<sup>r</sup>

<sup>a</sup>Dipartimento di Fisica, Università degli Studi e INFN, Milano 20133, Italy

<sup>b</sup>Chemical Engineering Department, Princeton University, Princeton, NJ 08544, USA

<sup>c</sup>University of Hamburg, Hamburg, Germany

<sup>d</sup>INFN Laboratori Nazionali del Gran Sasso, Assergi 67010, Italy

<sup>e</sup>Physics Department, Virginia Polytechnic Institute and State University, Blacksburg, VA 24061, USA

<sup>f</sup>Physics Department, University of Massachusetts, Amherst 01003, USA

<sup>g</sup>Physics Department, Princeton University, Princeton, NJ 08544, USA

<sup>h</sup>Lomonosov Moscow State University Skobeltsyn Institute of Nuclear Physics, Moscow 119234, Russia

<sup>i</sup>Department of Physics, University of Houston, Houston, TX 77204, USA

<sup>j</sup>St. Petersburg Nuclear Physics Institute, Gatchina 188350, Russia

<sup>k</sup>NRC Kurchatov Institute, Moscow 123182, Russia

<sup>l</sup>Joint Institute for Nuclear Research, Dubna 141980, Russia

<sup>m</sup>APC, Univ. Paris Diderot, CNRS/IN2P3, CEA/Irfu, Obs. de Paris, Sorbonne Paris Cité, France

<sup>n</sup>Max-Planck-Institut für Kernphysik, Heidelberg 69029, Germany

<sup>o</sup>Physik Department, Technische Universität München, Garching 85747, Germany

<sup>p</sup>Institute for Nuclear Research, Kiev 03680, Ukraine

<sup>q</sup>Dipartimento di Fisica, Università e INFN, Genova 16146, Italy

<sup>r</sup>M. Smoluchowski Institute of Physics, Jagellonian University, Crakow, 30059, Poland

<sup>s</sup>Dipartimento di Chimica, Università e INFN, Perugia 06123, Italy

<sup>t</sup>Physics and Astronomy Department, University of California Los Angeles (UCLA), Los Angeles, CA 90095, USA

**Abstract.** The solar neutrino experiment Borexino, which is located in the Gran Sasso underground laboratories, is in a unique position to study muon-induced backgrounds in an organic liquid scintillator. In this study, a large sample of cosmic muons is identified and tracked by a muon veto detector external to the liquid scintillator, and by the specific light patterns observed when muons cross the scintillator volume. The yield of muon-induced neutrons is found to be  $Y_n = (3.10 \pm 0.11) \cdot 10^{-4} n / (\mu \cdot (\text{g}/\text{cm}^2))$ . The distance profile between the parent muon track and the neutron capture point has the average value  $\lambda = (81.5 \pm 2.7)$  cm. Additionally the yields of a number of cosmogenic radioisotopes are measured for  $^{12}\text{N}$ ,  $^{12}\text{B}$ ,  $^8\text{He}$ ,  $^9\text{C}$ ,  $^9\text{Li}$ ,  $^8\text{B}$ ,  $^6\text{He}$ ,  $^8\text{Li}$ ,  $^{11}\text{Be}$ ,  $^{10}\text{C}$  and  $^{11}\text{C}$ . All results are compared with Monte Carlo simulation predictions using the FLUKA and GEANT4 packages. General agreement between data and simulation is observed for the cosmogenic production yields with a few exceptions, the most prominent case being  $^{11}\text{C}$  yield for which both codes return about 50% lower values. The predicted  $\mu$ -n distance profile and the neutron multiplicity distribution are found to be overall consistent with data.

**Keywords:** Borexino, Muon, Cosmic, Cosmogenic, Neutron

## 1 Introduction

The Borexino experiment is a 278 t liquid-scintillator detector designed for real-time measurements of low energy ( $<20$  MeV) neutrinos. The primary goal of the experiment is the spectroscopy of solar neutrinos. In this respect Borexino has performed a precision measurement of the  $^7\text{Be}$  neutrino line [1, 2], has lowered the threshold for the real-time detection of the  $^8\text{B}$  neutrino spectrum to 3 MeV [3], and has directly observed the neutrinos of the pep line, at the same time placing the most stringent limit on the CNO neutrino flux [4]. Borexino is also very competitive in the detection of anti-neutrinos ( $\bar{\nu}$ ), having reported a first observation of geo-neutrinos in 2010 [5], followed by a recent new measurement [6]. Finally, the experiment is sensitive to neutrino signals from a galactic core-collapse supernova [7, 8].

The extremely low background in the scintillator target is essential to the success of Borexino. While careful pre-selection of detector materials and extensive purification of the organic scintillator is necessary, shielding from external, and especially cosmic, radiation is

of comparable importance. The detector is located deep underground (3800 meters of water-equivalent, m w.e.) in the Hall C of the Laboratori Nazionali del Gran Sasso (LNGS, Italy), where the cosmic muon flux is suppressed by about six orders of magnitude. In spite of this large attenuation factor, residual muons constitute an important source of background for neutrino detection. For example, they produce neutrons or radioactive isotopes by spallation reactions in target materials, *e.g.*  $^{12}\text{C}$ , and these produce signals which mimic the observation of a reaction of interest.

An understanding and mitigation of muon-induced backgrounds are of great relevance to all investigations of rare processes. In the majority of underground rare-event experiments, muons and their spallation products constitute a severe source of background. For example, in direct dark matter searches, neutron interactions feature a signature very similar to those induced by WIMPs, and careful shielding must be employed. In  $0\nu\beta\beta$  experiments, the  $\beta$ -decays of long-lived radioisotopes produced in-situ can be significant background components. It is expected that cosmogenic backgrounds will be even more important in the next generation of low-background experiments, as the detector sizes and sensitivities are increasing. Thus more sophisticated muon vetoes as well as extensive shielding will be necessary.

This paper presents the results of a detailed investigation of muons, and especially their spallation products, which were detected by Borexino. Due to its simple geometry, large mass, and excellent event reconstruction capability, Borexino offers the unique possibility for a precise study of cosmogenic production inside a large, uniform volume of low-Z material. The paper is structured as follows. After introducing the detector layout and the general cosmic background conditions found at the LNGS facility (section 2), we review the results of the cosmic muon flux and present the reconstructed angular distribution of the muons (section 3). We continue with a detailed study of the neutron production rate and multiplicity in liquid scintillator (section 4). We also present the lateral distance profile of neutron captures with respect to the parent muon track. This is of special interest for dark matter experiments relying on low-Z materials for neutron shielding. Moreover, we investigate the production of a selection of cosmogenic radioisotopes in the scintillator volume (section 5). Finally, we perform a detailed comparison of our experimental results with the rates and profiles predicted by the commonly used FLUKA and GEANT4 simulation codes (section 6). This validity check is of considerable importance as Monte Carlo simulations represent virtually the only means to transfer our findings to the various detector geometries realized in other low-background experiments. We also show the production yields determined in the KamLAND experiment [9] which features a setup largely comparable to Borexino. Section 7 summarizes our main results.

## 2 The Borexino Detector at the LNGS

The Borexino detector [10] consists of a spherical inner detector (ID) containing a liquid scintillator target and a surrounding outer detector (OD) consisting of a large water tank. This tank acts both as passive shield and as an active muon veto. The general layout is presented in figure 1. The central, active scintillator consists of pseudocumene (PC, 1,2,4-trimethylbenzene), doped with 1.5 g/liter of PPO (2,5-diphenyloxazole, a fluorescent dye). The nominal target mass is 278 t. The scintillator is contained in a thin (125  $\mu\text{m}$ ) nylon vessel of 4.25 m radius and is shielded by two concentric inactive PC buffers (323 t and 567 t) doped with few g/l of a scintillation light quencher (dimethylphthalate). The two PC buffers are separated by a second thin nylon membrane to prevent diffusion of radon towards the

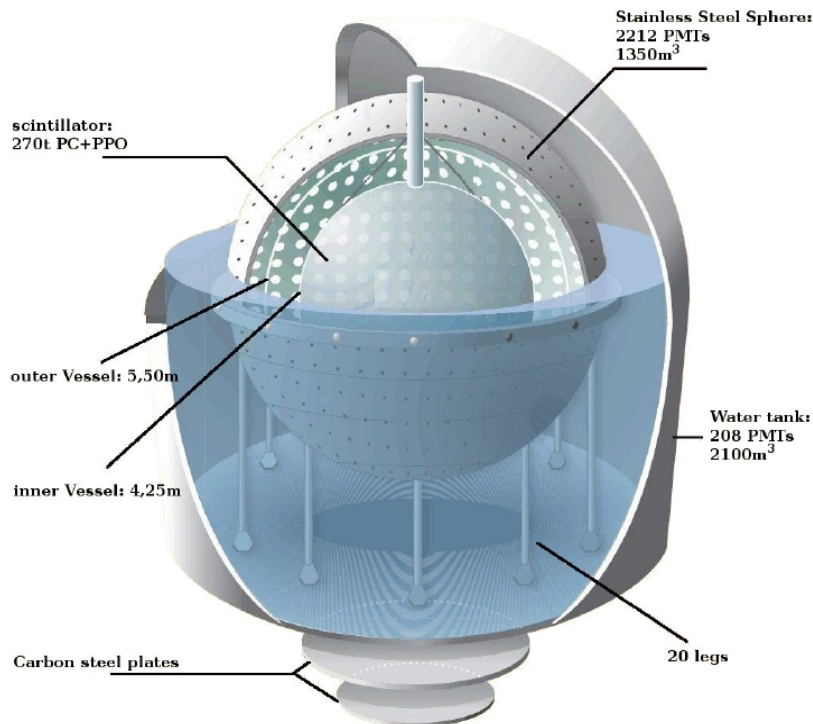


**Figure 1.** Sketch of the Borexino detector.

scintillator. The scintillator and buffers are contained in a Stainless Steel Sphere (SSS) with a diameter of 13.7 m. The SSS is enclosed in a 18.0 m diameter, 16.9 m high domed Water Tank (WT), containing 2100 t of ultra-pure water. The scintillation light is detected via 2212 8" -photomultiplier tubes (PMTs) uniformly distributed on the inner surface of the SSS. Additional 208 8" PMTs instrument the WT and detect the Cherenkov light radiated by muons in the water shield [11].

In Borexino, low energy neutrinos ( $\nu$ ) of all flavors are detected by means of their elastic scattering off electrons or, in case of electron anti-neutrinos ( $\bar{\nu}_e$ ), via the inverse  $\beta$  decay on free protons. The electron (positron) recoil energy is converted into scintillation light which is then collected by the ID PMTs. Borexino is sensitive to neutrinos of at least 100 keV in energy, while the inverse  $\beta$  decay induced by anti-neutrinos requires a minimum neutrino energy of 1.8 MeV. While cosmic muons crossing the ID deposit much greater energies and create substantially more light, cosmogenic neutrons and radioisotopes induce scintillation signals on a scale similar to neutrino interactions.

### 3 Cosmic Muons

The primary cosmic muon flux arriving at Earth's surface ( $6.5 \cdot 10^5 \mu / (\text{m}^2 \cdot \text{h})$ ) is strongly attenuated when penetrating the mountain above the detector by about a factor  $10^6$ . The rock shielding is equivalent to some 3800 m of water. Thus the mean energy of the muons at LNGS site is about 280 GeV, compared to about 1 GeV at the surface, since the lower energy

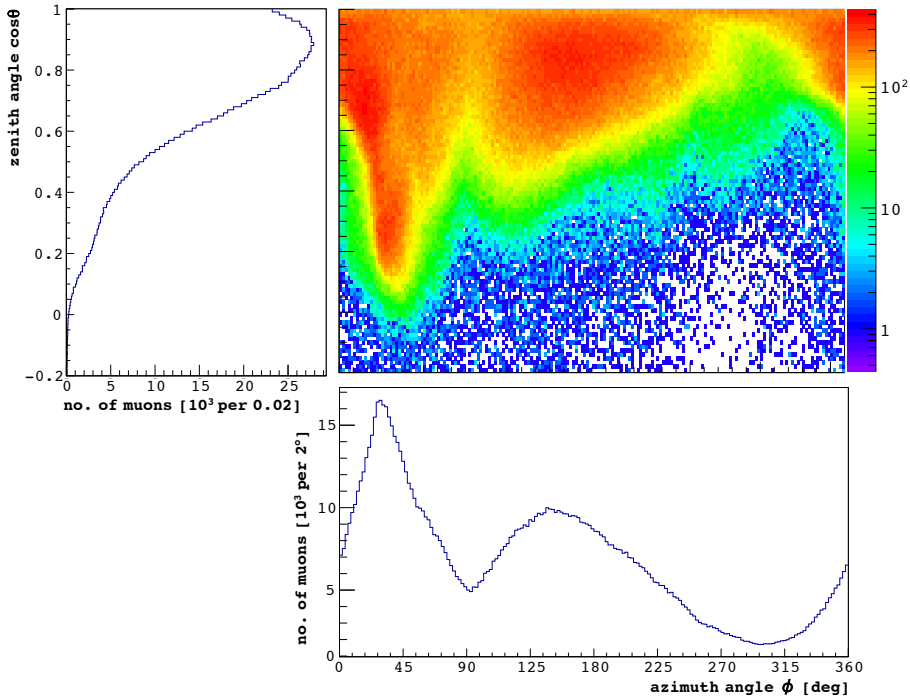


**Figure 2.** Angular distribution of the muons crossing the Borexino IV. The side plots show the projections to astronomic azimuth and zenith angles.

muons incident at the surface are absorbed, and the spectrum steeply falls as a function of energy [12].

We consider in this article only muons generating signals in both the ID and the OD for which track reconstruction is also performed. Muons identification occurs with three different methods [11]. The first two are based on the detection of the Cherenkov light produced in the water. In the first method, the light triggers the OD sub-system (muon trigger flag, MTF). In the second method, a cluster of OD PMT pulses is identified, correlated in space and time (muon cluster flag, MCF). The third method relies on pulse shape identification of muon tracks among the point-like scintillation events detected by the ID (inner detector flag, IDF). The detection efficiencies are 0.9925(2), 0.9928(2) and 0.9890(1) respectively. The cosmic muon interaction rate in Borexino was found in [13] to be  $(4310 \pm 2_{\text{stat}} \pm 10_{\text{syst}}) \text{d}^{-1}$  and corresponds to a flux of  $(3.41 \pm 0.01) \cdot 10^{-4} \text{m}^{-2}\text{s}^{-1}$  as measured in Hall C of the LNGS laboratory.

The Borexino ID features a uniform acceptance for incident cosmic muons which is independent of the arrival directions, thanks to its spherical symmetry. The observed angular distribution is shown in figure 2 as a function of the astronomic azimuth ( $\phi$ ) and zenith ( $\theta$ ) angles in a two-dimensional contour plot<sup>1</sup>. In addition, the one-dimensional projections on the  $\theta$  and  $\phi$ -planes are also presented. All three distributions reflect the influence of the local mountain topology: The differences in the thickness of the overlaying rock are imprinted as angle-dependent variations in the residual muon flux. Note that due to its uniform detection

<sup>1</sup>A table listing the numerical values of the distribution has been included in the supplementary materials.

efficiency, Borexino is in a unique position to map the muon distribution at depth close to the horizon without angular distortions.

To obtain these plots, the ID tracking algorithm described in [11] was employed. These plots consider only muons crossing the IV because their tracks offer the best angular resolution. For this selection, the (redundant) requirements of a reconstructed energy deposition of at least 300 MeV in the IV and an impact parameter of less than 4.25 m were applied. The remaining sample consists of 1 221 470 individual muon tracks.

## 4 Cosmogenic Neutrons

Cosmic muons crossing the detector produce fast neutrons through different spallation processes on carbon nuclei. The neutron velocities are slowed in the scintillator by collisions with hydrogen or carbon nuclei to thermal sub-eV energies in a few scatterings. This process occurs within a few tens of ns. Consequently, signals from ionizations due to the recoiling nuclei cannot be disentangled from the much higher light emission of an incident muon. For the same reason, fast neutron captures are also not visible. About 1% of the neutrons are captured during a fast capture process, as determined by our Monte Carlo simulations. We do not correct our results to account for this effect in this paper, and hereafter we refer to all neutron captures as due to slower thermal capture. The mean capture time of a thermal neutron in the liquid scintillator is  $\sim 250 \mu\text{s}$ , and the subsequent gamma-ray emission is distinctly visible. The energy emitted in gamma rays is 2.2 MeV if the neutron is captured on hydrogen and 4.9 MeV if captured on carbon. Based on the elemental composition of the scintillator and the relative capture cross-sections, about 99% of all thermal neutron captures are expected on hydrogen [14]. The ability of Borexino to detect cosmogenic neutrons was described in detail in [11].

### 4.1 Neutron detection with the main electronics

The data acquisition system issues a dedicated neutron acquisition gate of 1.6 ms length after a muon crosses the SSS. The captured PMT pulses are due to neutron capture-gammas and accidental  $^{14}\text{C}$  decays. The latter is an intrinsic contaminant of the scintillator. Particular care must be taken when the muon crosses the scintillator because of the large amount of visible light which is created. For these events, the baseline of the front-end electronics takes up to  $30 \mu\text{s}$  to stabilize. Furthermore as a result of the intense PMT illumination, the front of the acquisition gate is highly populated by noise pulses creating a variable baseline on which the other pulses are superimposed. Thus the active time window for the analysis is set after the baseline stabilizes ( $30 \mu\text{s}$ ). An ad-hoc algorithm detects physical events by identifying *clusters* of time-correlated PMT pulses on top of the baseline with high efficiency. An energy threshold of 1.3 MeV is imposed via a variable selection cut based on detector saturation. The overall detection efficiency above threshold was determined using neutron samples which were selected as described below. The result is  $\varepsilon_{\text{det}} = (91.7 \pm 1.7_{\text{stat}} \pm 0.9_{\text{syst}}) \%$  for cosmogenic neutrons captured later than  $30 \mu\text{s}$  after their parent muon is observed. The error incorporates the uncertainty in the threshold definition of the energy.

The data sample used for the analysis contains 559 live days, covering the time period from January 6, 2008, until February 2, 2010. The respective average scintillator volume contained in the nylon vessel was measured to be  $(306.9 \pm 2.9) \text{m}^3$ , or  $(22.8 \pm 0.2) \%$  of the SSS volume. This translates into an active mass of  $(270.2 \pm 2.6) \text{t}$ . The volume in which neutron captures are detected is not identical with that defined by the physical vessel

boundaries. For example, gamma-rays generated in the buffer close to the nylon vessel may cross into the scintillator volume and create a sizeable light output, while gamma-rays from neutron captures inside the scintillator may escape into the buffer undetected. This effect was quantified using a Monte Carlo simulation of neutron capture gammas in both buffer and scintillator. The simulation included the transport of scintillation light and electronic effects. Of all  $\gamma$ 's generated inside the SSS, the fraction of events which deposit more than 1.3 MeV energy in the IV,  $\varepsilon_{\text{vol}}$ , is  $(23.0 \pm 0.3) \%$  for captures on hydrogen, and  $(24.2 \pm 0.2) \%$  for captures on carbon. Both the physical volume evaluation and the Monte Carlo simulation take into account variations in actual vessel shape and size over the data collection period.

The neutron capture time and the purity of the sample were studied based on the time difference ( $\Delta t$ ) between the occurrence of candidate clusters and their parent muons. The  $\Delta t$  distribution is fit by the sum of an exponential decay and a flat component for uncorrelated events. The resulting neutron capture time is  $\tau_n = (259.7 \pm 1.3_{\text{stat}} \pm 2.0_{\text{syst}}) \mu\text{s}$ , and is in agreement with our previous measurement [11]. Based on this value, the fraction of neutrons captured later than 30  $\mu\text{s}$  after the parent muon is  $\varepsilon_t = (89.1 \pm 0.8) \%$ . The contamination by uncorrelated events is found to be  $(0.5 \pm 0.2) \%$ .

## 4.2 Neutron detection with waveform digitizers

The Borexino detector is equipped with auxiliary DAQ systems based on fast waveform digitizers. Two of these systems (hereafter SYS1 and SYS2) were used in this analysis to evaluate the neutron detection efficiency  $\varepsilon_{\text{det}}$  of the main data acquisition system. Furthermore, these two systems provide a cross check on the neutron yield measurement (section 4.3).

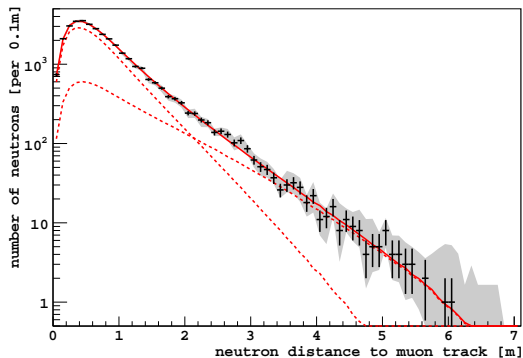
SYS1 is a single channel 500 MHz, 8 bit digitizer (Acqiris DP235) which records the cumulative analog output of all ID PMTs. It is triggered by the MTF condition of the outer detector, and collects data for about 1.6 ms. A cluster-finding algorithm identifies gamma-ray capture signals between 30 and 1590  $\mu\text{s}$  after muon detection. An energy threshold of 1.3 MeV is applied to reject noise pulses. SYS1 collected data between April 2008 and November 2009. The fit to the  $\Delta t$  distribution returns a capture time of  $(261 \pm 1_{\text{stat}} \pm 1_{\text{syst}}) \mu\text{s}$ . An additional flat component which would be allowed by the fit is consistent with zero at the  $1\sigma$  confidence level.

SYS2 is an auxiliary hardware architecture, based upon 96 waveform digitizers (CAEN v896: 400 MHz, 8 bit). Each channel receives the analog sum of 16 or 24 PMTs. The system operates independently from the main DAQ. A separate trigger is implemented by an FPGA unit (CAEN v1495). Data used for this analysis were collected between December 2009 and March 2012. A neutron detection efficiency of essentially 100 % is reached for an energy threshold above 1 MeV. For SYS2, the fit to the  $\Delta t$  distribution returns a capture time of  $(258.7 \pm 0.8_{\text{stat}} \pm 2.0_{\text{syst}}) \mu\text{s}$ . A residual of uncorrelated background on the level of  $(0.5 \pm 0.1) \%$  was determined by a fit and when using a delayed time window.

The values of the capture time obtained by SYS1 and SYS2 are in good agreement with the values using the main electronics (section 4.1).

## 4.3 Neutron production rate and multiplicity

The data set acquired by the main DAQ contains a sample of  $N_\mu = 2\,384\,738$  muons and  $N_n = 111\,145$  neutrons. The neutron capture rate for the efficiencies described above, is determined to  $R_n = (90.2 \pm 2.0_{\text{stat}} \pm 2.4_{\text{syst}}) (\text{d } 100\text{t})^{-1}$  after scaling. The systematic uncertainty of this measurement is dominated by the neutron capture time and the average scintillator volume contained inside the IV.



parameter	fit value
$\sigma_{\text{muon}}$ [cm]	$33.6 \pm 0.6 \pm 0.6$
$\mu_{\text{muon}}$ [cm]	$23.8 \pm 0.6 \pm 0.6$
$\lambda_{\text{short}}$ [cm]	$61.2 \pm 0.6 \pm 2.6$
$f_{\text{short}}$ [%]	$76.5 \pm 0.5 \pm 5.5$
$\lambda_{\text{long}}$ [cm]	$147 \pm 3 \pm 12$
$f_{\text{long}}$ [%]	$23.5 \pm 0.4 \pm 5.5$

**Figure 3.** The muon-neutron distance distribution observed in Borexino: black crosses represent the data points for the standard neutron hit multiplicity cut. The shaded-grey area indicates the systematic uncertainty. The fit of the toy Monte Carlo is indicated by the solid red line. The dashed lines correspond to two exponential components, each featuring a decay length  $\lambda$  and a relative fraction  $f$ . The muon resolution parameters  $\mu$  and  $\sigma$  are left free in the fit procedure (see sect. 4.4 and [11] for details). The table lists the best-fit results with statistical and systematic uncertainties. The fit returns  $\chi^2/\text{ndf} = 57/54$ .

The rate of muons which produce neutrons that eventually are captured inside the IV, is  $R_n^\mu = (67.5 \pm 0.4_{\text{stat}} \pm 0.2_{\text{syst}}) \text{d}^{-1}$  ( $\sim 1.5\%$  of muons crossing the ID). The detector-specific ratio  $R_n/R_n^\mu$  corresponds to an average neutron multiplicity within the IV volume of  $\bar{M} = (3.61 \pm 0.08_{\text{stat}} \pm 0.07_{\text{syst}}) n/\mu$ . The distribution of the multiplicities of detected neutron captures is shown in figure 13 where it is compared to Monte Carlo predictions. The neutron yield per unit length of muon track in the target medium is

$$\begin{aligned}
 Y_n &= \frac{N_n}{N_\mu} \cdot \frac{1}{\ell_\mu^{\text{avg}}} \cdot \frac{1}{\rho_{\text{scint}}} \cdot \frac{1}{\varepsilon_{\text{det}} \cdot \varepsilon_{\text{t}} \cdot \varepsilon_{\text{vol}}} \\
 &= (3.10 \pm 0.07_{\text{stat}} \pm 0.08_{\text{syst}}) \cdot 10^{-4} n/(\mu \cdot (\text{g}/\text{cm}^2))
 \end{aligned} \tag{4.1}$$

where  $\ell_\mu^{\text{avg}} = 4/3 R_{\text{SSS}}$  is the average muon path through the SSS with  $R_{\text{SSS}} = (6.821 \pm 0.005) \text{m}$  and  $\rho_{\text{scint}} = 0.88 \text{g}/\text{cm}^3$  is the scintillator density. We chose to consider the muon path through the SSS and not just the IV and to include the ratio of the two volumes in  $\varepsilon_{\text{vol}}$  in order to correctly account for the effective neutron detection volume. This is discussed in section 4.1. The statistical uncertainty associated with this result has been assessed by a toy Monte Carlo code which simulates neutron production by muons in order to observe the size of the fluctuations. For varying values of the muon rate, the statistical uncertainty is approximately seven times the square root of the number of neutron captures divided by the live time. This results in a statistical uncertainty of 3%.

As a consistency check, the neutron yield has been also determined based on the waveform digitizers:  $Y_n^{\text{SYS1}} = 3.19 \pm 0.08_{\text{stat}} \pm 0.10_{\text{syst}}$  for SYS1 and  $Y_n^{\text{SYS2}} = 2.87 \pm 0.07_{\text{stat}} \pm 0.15_{\text{syst}}$  for SYS2 in units of  $10^{-4} n/(\mu \cdot (\text{g}/\text{cm}^2))$ . This is in reasonable agreement with the value given in equation (4.1).

#### 4.4 Neutron lateral distance

Borexino can spatially reconstruct the emission point of the neutron capture gamma-ray as well as the track of its parent muon. This information may be used to compute the shortest



(perpendicular) distance between the neutron vertex and the parent muon track (hereafter: neutron lateral distance). A toy Monte Carlo was fit to the data in order to separate the distance travelled by the neutrons from resolution effects of the detector (see below).

Muon track and neutron vertices were reconstructed based on the Borexino main DAQ in order to obtain the lateral distance distribution from the data. Only muons and neutrons having a radial distance less than 4 m from the detector center were selected in order to ensure a well-defined geometry for comparison to the Monte Carlo. Moreover, the samples were cleaned to remove tracks and vertices of inferior reconstruction quality. In case of the muons, only events which feature spatially compatible tracks in both sub-detectors are used. The neutron selection cuts are much more restrictive. Due to electronic effects and PMT afterpulses which were present after very luminous muons, the spatial reconstruction of subsequent neutron events can be severely compromised. This results in systematic shifts increasing or decreasing the distance between the neutron capture point and the parent muon track [11]. Systematic studies demonstrated that the majority of these effects (e.g. afterpulses) subside in the first 200  $\mu\text{s}$  after a muon event. At later times, a fraction of the electronic channels might be affected by buffer overflow, which leads to asymmetric PMT hit patterns. Therefore, only neutron captures with a minimum time delay of 200  $\mu\text{s}$  are compared to a parent muon with the further restriction that the neutron event was composed of at least 100 individual PMT signals in order to ensure an unbiased vertex reconstruction ( $N_{\text{hits}} > 100$ ). The latter condition is easily met by neutrons produced by minimum-ionizing muons, but depletes the sample of useful neutron captures in case of very luminous muon events. Such muons are expected to create extensive hadronic showers, and there is a risk that the hit multiplicity cut for the neutrons introduces a bias to the selected sample which preferentially suppresses neutrons at large distances from their parent tracks. Finally, we limit the visible energy window to  $E_{\text{vis}} \in [0.9; 4.8] \text{ MeV}$  in order to select only neutron captures on hydrogen and carbon, while removing a minor contamination from short-lived cosmogenic isotopes. The combination of cuts reduces the remaining sample to  $\sim 20\%$  of the original neutrons.

The resulting lateral distance distribution is shown in figure 3. The grey shaded area corresponds to the systematic uncertainty introduced by the cut  $N_{\text{hits}} > 100$ , and was obtained by varying the minimum  $N_{\text{hits}}$  condition for neutron selection from 0 to 200. Due to the broad initial energy spectrum of the spallation neutrons and the corresponding distribution of the neutron mean free paths, a simple exponential law proves insufficient to reproduce the distribution. We find that at least two exponential components ( $\lambda_{\text{short}}$  and  $\lambda_{\text{long}}$ ) are required for a satisfactory description of the data. The fit function shown in figure 3 was obtained by a toy Monte Carlo simulation. Apart from the exponential components, the fit takes into account the muon and neutron spatial resolutions, which includes the average displacement of the neutrons during thermalization and the finite propagation distance of the capture gamma in scintillator ( $\sim 20 \text{ cm}$ ). The geometric impact of the applied radial cuts described above are included. The muon lateral resolution is described by a Gaussian smearing  $\sigma$  with a constant radial offset  $\mu$ . These are free parameters in the fit. Conversely, the neutron vertex resolution is set to a fixed value of 23 cm (see [11] for details).

The fit returns a short component  $\lambda_{\text{short}} = (61.2 \pm 0.6_{\text{stat}} \pm 2.6_{\text{syst}}) \text{ cm}$  which is in agreement with earlier LVD results [15]. The long component is found to be  $\lambda_{\text{long}} = (147 \pm 3_{\text{stat}} \pm 12_{\text{syst}}) \text{ cm}$ . Systematic uncertainties for the parameters were determined by multiple repetitions of the fit while varying the minimum  $N_{\text{hits}}$  condition for the neutrons. Based on the relative weights of the two effective components, an average lateral distance of  $\lambda = (81.5 \pm 2.7) \text{ cm}$  was determined.

Cosmogenic Isotope	Lifetime	Q-Value [MeV]	Decay Type	Cosmogenic Isotope	Lifetime	Q-Value [MeV]	Decay Type
<sup>12</sup> N	15.9 ms	17.3	$\beta^-$	<sup>6</sup> He	1.16 s	3.51	$\beta^-$
<sup>12</sup> B	29.1 ms	13.4	$\beta^+$	<sup>8</sup> Li	1.21 s	16.0	$\beta^-$
<sup>8</sup> He	171.7 ms	10.7	$\beta^-$	<sup>11</sup> Be	19.9 s	11.5	$\beta^-$
<sup>9</sup> C	182.5 ms	16.5	$\beta^+$	<sup>10</sup> C	27.8 s	3.65	$\beta^+$
<sup>9</sup> Li	257.2 ms	13.6	$\beta^-$	<sup>11</sup> C	29.4 min	1.98	$\beta^+$
<sup>8</sup> B	1.11 s	18.0	$\beta^+$				

**Table 1.** List of cosmogenic isotopes expected to be produced by muons in organic scintillators in measurable rates.

## 5 Cosmogenic Radioisotopes

In addition to neutrons, radioactive isotopes are produced in muon-induced spallation processes on the target nuclei. A list of the relevant cosmogenic isotopes with their properties and sorted by increasing lifetime can be found in table 1.

Candidate events are selected via two observables: the visible energy,  $E$ , and the time difference,  $\Delta t$ , with respect to a parent muon. The distributions of the two observables are fit simultaneously in an unbinned likelihood fit. However, matching to a parent muon is not unique in general, as many muons can be present within the selected analysis time gate  $t_g$ . This results in multiple values of  $\Delta t$  for a given candidate, with only one muon physically correlated with the neutron decay. This effect is most prominent for the analyses on cosmogenic isotopes with lifetimes on the order of seconds or longer since in average cosmic muons cross the ID every 20 s. The distribution in  $\Delta t$  is fit with the function:

$$F(\Delta t) = \sum_i \frac{N_i^t}{\tau_i} e^{-\frac{\Delta t}{\tau_i}} + \frac{N_b^t}{t_g} + \frac{N_{um}^t}{t_g} \quad (5.1)$$

The number of decays in each isotope profile is  $N_i^t$  with  $\tau_i$  its lifetime. Flat contributions,  $N_b^t$  and  $N_{um}^t$ , account for uncorrelated background events and for physically uncorrelated matches, respectively. The latter is a property of the selected data set and calculated independently. The fit function is valid for time scales much shorter than the average run duration of a data set ( $\sim 6$  h). This is valid for all cosmogenic isotopes with the exception of <sup>11</sup>C (table 1). As will be presented in section 5.7, a distortion of the time profile due to run-boundary effects can be avoided by a time cut of candidate events which occur close to run-start. The spectral shapes of the respective isotopes are generated with the GEANT4 based Borexino Monte Carlo code. The simulation reproduces the full detector response, yielding about 500 photoelectrons/MeV of deposited energy in  $\beta$  and  $\gamma$  decays, and spectral fits can be performed directly on the number distribution of photoelectrons from candidate events. For easier reference, this conversion factor will be used to refer to the energy selection cuts in the [MeV] units in the following analyses. Based on the visible energy  $E$  of an event, the spectral fit function  $G(E)$  is given by:

$$G(E) = \sum_i N_i^E g_i(E) + N_b^E g_b(E) \quad (5.2)$$

The spectral shapes of the analyzed isotopes are denoted by  $g_i(E)$  with the respective number of decays  $N_i^E$ . The uncorrelated background is addressed with the spectral shape  $g_b(E)$  and

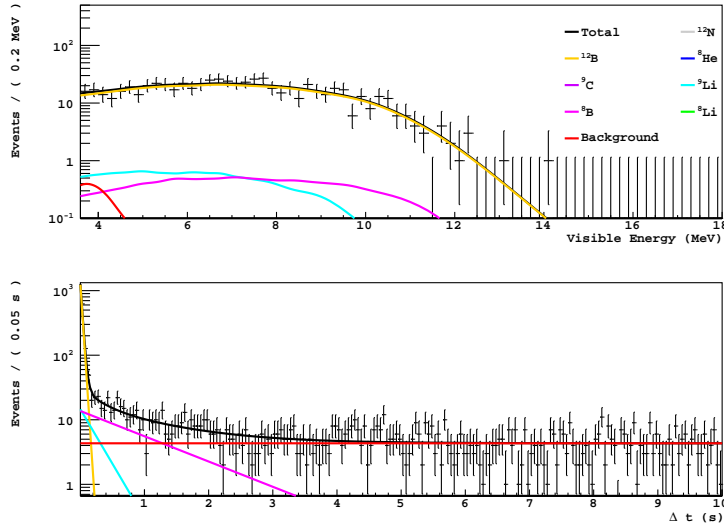


**Figure 4.** Simultaneous fit of the cosmogenic isotopes  $^{12}\text{N}$  and  $^{12}\text{B}$  in visible energy deposition (top panel) and decay time relative to preceding muons (bottom panel), including the isotopes  $^8\text{He}$  (blue),  $^9\text{C}$ ,  $^9\text{Li}$ ,  $^8\text{B}$  and  $^8\text{Li}$  as contaminants. The fit returns only upper limits for the isotopes  $^{12}\text{N}$ ,  $^8\text{He}$ ,  $^9\text{C}$  and  $^8\text{Li}$ , and they cannot be seen in the graph. The goodness of the simultaneous fit is  $\chi^2/\text{ndf} = 348/236$ .

$N_b^E$  is the number of entries. The energy distribution is generated from events which occur within a time interval,  $t_E$ , relative to preceding muons. To enhance the signal to noise ratio,  $t_E$  is chosen to be in the order of the lifetimes of the respective cosmogenic radionuclides. The number of isotope decays in the time and energy fit ( $N_i^t$  and  $N_i^E$ ), and the background events ( $N_b^t$  and  $N_b^E$ ), are related to the known selection cut efficiencies in time and energy.

Most cosmogenic isotopes are expected to be produced at a very low rate. To reduce accidental coincidences, muons are removed from the sample of candidate isotope events by the application of the MTF and IDF muon identification methods (section 3). The efficiency and small distortions due to the application of IDF are included in the Monte Carlo generated spectral shapes. MTF efficiency is accounted for *a posteriori*. Unless stated otherwise, the positions of candidate events are also required to lie within a *fiducial volume* (FV). This is defined by a sphere of a 3 m radius which corresponds to a 99.6 t mass of liquid scintillator. The systematic uncertainty in the reconstructed volume for the decay energies of interest is estimated to  $\pm 3.8\%$  and contributes to the uncertainty of all measured yields. Except where differently noted, the analyses on cosmogenic radioisotopes are based on the same data set used for the neutron yield analysis (section 4.1).

### 5.1 $^{12}\text{N}$ and $^{12}\text{B}$

Candidate events for the decays of  $^{12}\text{N}$  ( $\beta^+$ -emitter,  $\tau = 15.9$  ms,  $Q = 17.3$  MeV) and  $^{12}\text{B}$  ( $\beta^-$ -emitter,  $\tau = 29.1$  ms,  $Q = 13.4$  MeV) are selected within an energy range  $E \in [3.6, 18]$  MeV and a time gate  $\Delta t \in t_g = [2 \text{ ms}, 10 \text{ s}]$  with respect to a preceding muon event. The energy distribution is constructed from events with  $\Delta t \in t_E = [2, 60]$  ms. This increases the signal-to-background ratio. After each muon, a 2 ms veto is applied to avoid muon-induced secondaries (mainly neutrons) which leads to a negligible dead time. Fur-

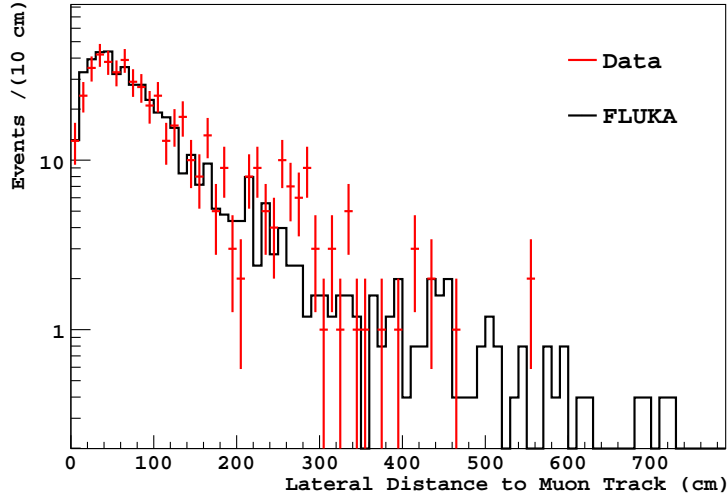


**Figure 5.** Comparison of measured and simulated lateral production profiles for cosmogenic  $^{12}\text{B}$  candidates inside the FV with respect to the parent muon track. For improved spatial resolution we select only tracks of muons which cross the IV at an impact parameter of less than 4 m.

thermore, decays of the cosmogenic isotopes  $^8\text{He}$ ,  $^9\text{C}$ ,  $^9\text{Li}$ ,  $^8\text{B}$  and  $^8\text{Li}$  are considered as contaminations and are fit alongside  $^{12}\text{N}$  and  $^{12}\text{B}$ . The upper limit of the time gate  $t_g$  (i.e. 10 s) is driven by the lifetimes of the isotopes  $^8\text{B}$  ( $\tau = 1.11$  s) and  $^8\text{Li}$  ( $\tau = 1.21$  s). In addition, a fraction of  $(86.2 \pm 0.2)\%$  of all  $^{11}\text{Be}$  decays is expected within the selected energy range. However, due to its low production rate and long lifetime ( $\tau = 19.9$  s), this contribution is estimated to be less than 1% in the time profile, and negligible in the energy distribution (section 5.5). The background spectral shape is built from events with  $\Delta t > 10$  s to avoid accidental coincidences of short-lived cosmogenic isotopes. Figure 4 shows the simultaneous fit in energy and time. The efficiency of the energy cut is evaluated via the Borexino Monte Carlo simulation to be  $\varepsilon(^{12}\text{N}) = (79.3 \pm 0.4)\%$  and  $\varepsilon(^{12}\text{B}) = (84.0 \pm 0.3)\%$ . The uncertainties are due to the detector energy resolution. The simultaneous fit yields a rate of  $R(^{12}\text{N}) < 0.03$  (d 100t) $^{-1}$  at a  $3\sigma$  confidence level, and  $R(^{12}\text{B}) = (1.62 \pm 0.07_{\text{stat}} \pm 0.06_{\text{syst}})$  (d 100t) $^{-1}$ . These translate to production yields of  $Y(^{12}\text{N}) < 1.1 \cdot 10^{-7} / (\mu \cdot (\text{g}/\text{cm}^2))$  and  $Y(^{12}\text{B}) = (55.6 \pm 2.5_{\text{stat}} \pm 2.1_{\text{syst}}) \cdot 10^{-7} / (\mu \cdot (\text{g}/\text{cm}^2))$ .

$^{12}\text{B}$  at a level of  $(94.6 \pm 0.3)\%$  of all events is clearly the dominating cosmogenic isotope within the selected time window ( $\Delta t \in [2, 60]$  ms). Figure 5 shows the lateral production profile of this isotope with respect to the reconstructed track of the parent muon.

## 5.2 $^8\text{He}$ and $^9\text{Li}$

Both  $\beta^-$ -emitters  $^8\text{He}$  ( $\tau = 171.7$  ms,  $Q = 10.7$  MeV) and  $^9\text{Li}$  ( $\tau = 257.2$  ms,  $Q = 13.6$  MeV) exhibit daughter nuclei with neutron-unstable excited states. With a 16% branching ratio, the  $\beta$ -decay of  $^8\text{He}$  populates such a state in  $^8\text{Li}$ . For  $^9\text{Li}$ , the branching ratio to a neutron-unstable state in  $^9\text{Be}$  is 51%. The subsequently emitted neutron is captured mainly on hydrogen with a mean capture time of  $(259.7 \pm 3.3)$   $\mu\text{s}$  (section 4.1), emitting a characteristic 2.2 MeV gamma-ray. The triple-coincidence of a muon, a  $\beta$ -emission, and a delayed neutron capture provides a very clean signature, which allows analysis of events within the entire

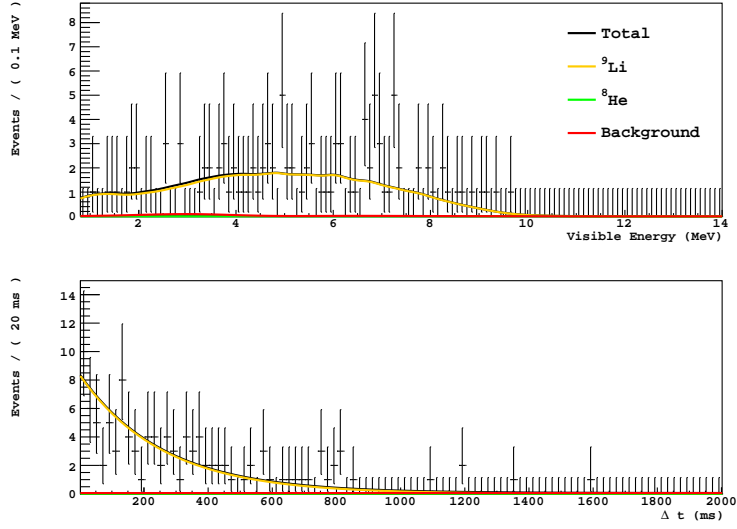


**Figure 6.** Simultaneous fit of the cosmogenic isotopes  $^8\text{He}$  and  $^9\text{Li}$  in visible energy deposition (top panel) and decay time relative to preceding muons (bottom panel). The fit returns only an upper limit for the isotope  $^8\text{He}$  and its line cannot be seen in the graph. The goodness of the simultaneous fit is  $\chi^2/\text{ndf} = 71/98$ .

mass of the inner vessel. Thus, an enlarged data set of 1366 live days taken between January 6, 2008, and August 31, 2012, is used for the analysis with a mean inner vessel mass of  $(268.2 \pm 2.8)$  t. The requirements for candidate events for the  $\beta$ -emissions are  $\Delta t \in [2 \text{ ms}, 2 \text{ s}]$  and  $E \in [0.8, 14] \text{ MeV}$ . The energy distribution is taken from events with  $\Delta t \in [2 \text{ ms}, 1 \text{ s}]$ . Subsequent neutron capture candidates are selected by  $E \in [1.7, 2.6] \text{ MeV}$ . These are required to occur within 1 m distance and a maximum time delay of 1.3 ms to a  $\beta$ -like event. The uncorrelated background spectrum is derived from events with  $\Delta t > 1 \text{ s}$ . Figure 6 shows the simultaneous fit in energy and time of  $^8\text{He}$  and  $^9\text{Li}$ . The  $\beta n$  selection cut efficiency has been evaluated to be  $\varepsilon(\beta n) = (79.3 \pm 0.4) \%$  via the Borexino Monte Carlo simulation. The energy cut efficiencies are estimated to be  $\varepsilon(^8\text{He}) = (99.49 \pm 0.05) \%$  and  $\varepsilon(^9\text{Li}) = (96.99 \pm 0.11) \%$ . The fit returns only an upper limit for  $^8\text{He}$ . Isotope production rates of  $R(^8\text{He}) < 0.042 (\text{d } 100\text{t})^{-1}$  at a  $3\sigma$  confidence level, and  $R(^9\text{Li}) = (0.083 \pm 0.009_{\text{stat}} \pm 0.001_{\text{syst}}) (\text{d } 100\text{t})^{-1}$  are observed. The corresponding yields are  $Y(^8\text{He}) < 1.5 \cdot 10^{-7} / (\mu \cdot (\text{g}/\text{cm}^2))$  and  $Y(^9\text{Li}) = (2.9 \pm 0.3) \cdot 10^{-7} / (\mu \cdot (\text{g}/\text{cm}^2))$ .

### 5.3 $^8\text{B}$ , $^6\text{He}$ and $^8\text{Li}$

The cosmogenic isotopes  $^8\text{B}$  ( $\beta^+$ -emitter,  $\tau = 1.11 \text{ s}$ ,  $Q = 18.0 \text{ MeV}$ ),  $^6\text{He}$  ( $\beta^-$ -emitter,  $\tau = 1.16 \text{ s}$ ,  $Q = 3.51 \text{ MeV}$ ) and  $^8\text{Li}$  ( $\beta^-$ -emitter,  $\tau = 1.21 \text{ s}$ ,  $Q = 16.0 \text{ MeV}$ ) feature similar lifetimes. However, the significantly lower  $Q$ -value of  $^6\text{He}$  enables a partial disentanglement of these radionuclides via cuts in visible energy and time. We separate the energy range in two regimes, denoted as ER1 ( $E \in [2, 3.2] \text{ MeV}$ ) and ER2 ( $E \in [5, 16] \text{ MeV}$ ), respectively. Regime ER1 comprises decays of all three isotopes, whereas ER2 includes only  $^8\text{B}$  and  $^8\text{Li}$ . The two energy intervals are fit simultaneously with their respective time profiles in a single, un-binned maximum likelihood fit. The spectral shape of uncorrelated background is derived from events with  $\Delta t > 140 \text{ s}$ . Table 2 summarizes the energy selection efficiencies and the

Energy regime	Time Gate $t_g$ [s]	Time Gate $t_E$ [s]	Cosmogenic Isotope	Lifetime [s]	Energy Cut Efficiency [%]
ER1 $E \in [2, 3.2]$ MeV	[1, 140]	[1, 2]	${}^8\text{B}$	1.11	$4.0 \pm 0.3$
			${}^6\text{He}$	1.16	$16.8 \pm 0.3$
			${}^8\text{Li}$	1.21	$8.1 \pm 0.2$
			${}^{10}\text{C}$	27.8	$77.1 \pm 0.2$
ER2 $E \in [5, 16]$ MeV	[1, 10]	[1, 3]	${}^8\text{B}$	1.11	$81.6 \pm 0.4$
			${}^8\text{Li}$	1.21	$67.5 \pm 0.4$

**Table 2.** Selection cuts of the candidate events in energy ( $E$ ) and time ( $t_g, t_E$ ) for the two regimes ER1 and ER2 for isotopes  ${}^8\text{B}$ ,  ${}^6\text{He}$  and  ${}^8\text{Li}$ . In addition, the expected cosmogenic isotopes are given with their lifetimes and energy cut efficiencies. For each energy regime, the time profile is constructed from events within the time interval  $t_g$  relative to preceding muons. To enhance the signal-to-background ratio, the energy distribution is based on events in the time interval  $t_E$ . The distributions and the result of a simultaneous fit in time and energy to both regimes is shown in figure 7.

chosen time gates for the time and energy distributions in these two energy regimes. Due to the lower energy threshold of ER1, an additional contribution of the cosmogenic isotope  ${}^{10}\text{C}$  ( $\beta^+$ -emitter,  $\tau = 27.8$  s,  $Q = 3.65$  MeV) is included as a free parameter in the fit. To avoid contaminations of short-living cosmogenic isotopes, a 1 s veto after each muon is applied for both regimes, inducing a dead time of 3.6 %. The result of the simultaneous fit is shown in figure 7 for the energy regimes ER1 and ER2, respectively. The isotope production rates are found to be  $R({}^8\text{B}) = (0.41 \pm 0.16_{\text{stat}} \pm 0.03_{\text{syst}}) (\text{d } 100\text{t})^{-1}$ ,  $R({}^6\text{He}) = (1.11 \pm 0.45_{\text{stat}} \pm 0.04_{\text{syst}}) (\text{d } 100\text{t})^{-1}$  and  $R({}^8\text{Li}) = (0.21 \pm 0.19_{\text{stat}} \pm 0.02_{\text{syst}}) (\text{d } 100\text{t})^{-1}$ . The corresponding yields are  $Y({}^8\text{B}) = (1.4 \pm 0.6_{\text{stat}} \pm 0.1_{\text{syst}}) \cdot 10^{-6} / (\mu \cdot (\text{g}/\text{cm}^2))$ ,  $Y({}^6\text{He}) = (3.80 \pm 1.53_{\text{stat}} \pm 0.14_{\text{syst}}) \cdot 10^{-6} / (\mu \cdot (\text{g}/\text{cm}^2))$  and  $Y({}^8\text{Li}) = (7.1 \pm 6.6_{\text{stat}} \pm 0.7_{\text{syst}}) \cdot 10^{-7} / (\mu \cdot (\text{g}/\text{cm}^2))$ .

#### 5.4 ${}^9\text{C}$

Candidate events for the decay of  ${}^9\text{C}$  ( $\beta^+$ -emitter,  $\tau = 182.5$  ms,  $Q = 16.5$  MeV) are selected by  $E \in [5, 18]$  MeV and  $\Delta t \in [250 \text{ ms}, 10.25 \text{ s}]$ . The lower energy threshold avoids decays of  ${}^6\text{He}$  in the data set. Events occurring for  $\Delta t \in [250, 600]$  ms are employed to obtain the energy distribution. After each muon, a 250 ms veto is applied, rejecting contributions from shorter-lived cosmogenic radionuclides and reducing the live time of the data set by 0.9 %. The isotopes  ${}^8\text{He}$ ,  ${}^9\text{Li}$ ,  ${}^8\text{B}$  and  ${}^8\text{Li}$  are treated as contaminants. Events for  $\Delta t > 10.25$  s are used to build the spectral shape of the uncorrelated background. The energy distribution for the  ${}^8\text{B}$ ,  ${}^6\text{He}$  and  ${}^8\text{Li}$  analysis (ER2 with  $E \in [5, 16]$  MeV,  $t_E \in [1, 3]$  s) is used to confine the rates of  ${}^8\text{B}$  and  ${}^8\text{Li}$  in the simultaneous fit as additional complementary information (section 5.3).

The result of the best fit for the time profile and both energy distributions is shown in figure 8. A fraction of  $\varepsilon({}^9\text{C}) = (73.4 \pm 0.4) \%$  of all  ${}^9\text{C}$  candidates is expected within the energy range of the  ${}^9\text{C}$  candidates. The rate and yield of  ${}^9\text{C}$  are determined to an upper limit of  $R({}^9\text{C}) < 0.47 (\text{d } 100\text{t})^{-1}$ , and  $Y({}^9\text{C}) < 1.6 \cdot 10^{-6} / (\mu \cdot (\text{g}/\text{cm}^2))$  at  $3\sigma$  confidence level after correcting for efficiencies.

#### 5.5 ${}^{11}\text{Be}$

Events with  $E \in [5, 12]$  MeV are chosen in order to determine production rate for  ${}^{11}\text{Be}$  which is a  $\beta^-$ -emitter, with  $\tau = 19.9$  s,  $Q = 11.5$  MeV. The lower energy boundary is needed in order to reject  ${}^{10}\text{C}$  and  ${}^{11}\text{C}$  decays as well as the external (uncorrelated)  $\gamma$ -background from  ${}^{208}\text{Tl}$ .

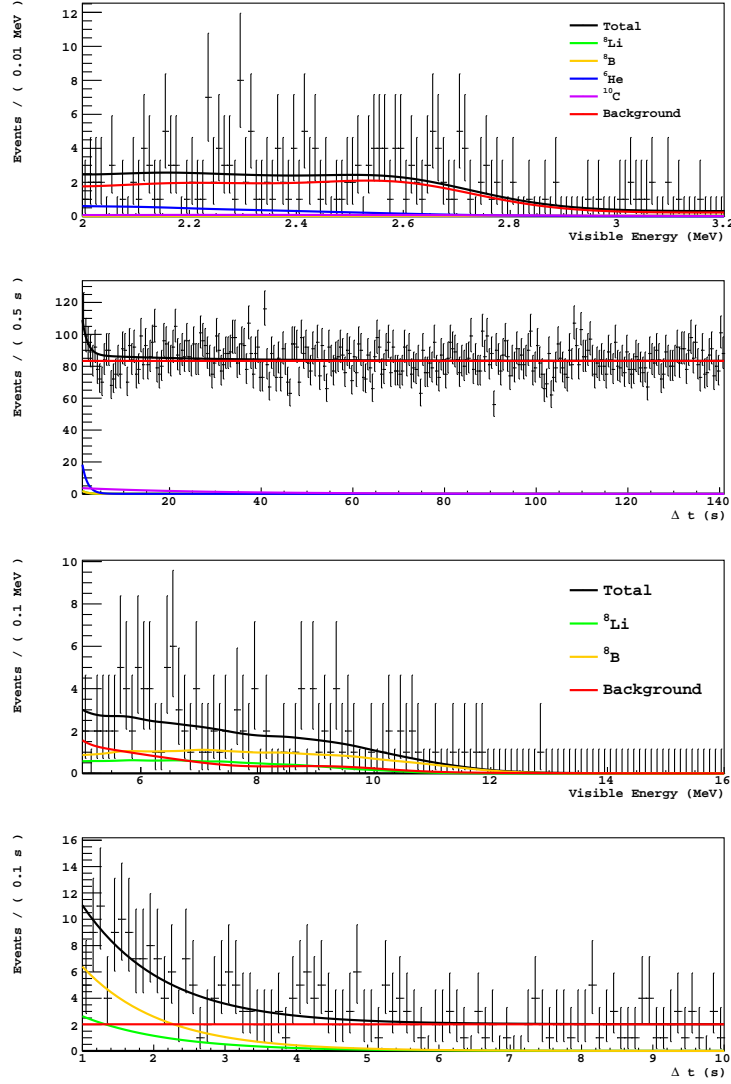


**Figure 7.** Simultaneous fit of the cosmogenic isotopes  $^8\text{B}$ ,  $^6\text{He}$  and  $^8\text{Li}$  in visible energy deposition (first and third panels) and decay time relative to preceding muons (second and fourth panels) for the energy regimes ER1 ( $E \in [2, 3.2]$  MeV) and ER2 ( $E \in [5, 16]$  MeV). The isotope  $^{10}\text{C}$  is included as contaminant. Some of the isotopes cannot be seen in the graph because the fit returns a very low value for their rates. The goodness of the simultaneous fit is  $\chi^2/\text{ndf} = 457/499$ .

The time profile is constructed for  $\Delta t \in [10, 210]$  s with respect to a preceding muon whose track is reconstructed within 1.5 m from the  $^{11}\text{Be}$  candidate decay. The energy distribution is composed of events with  $\Delta t \in [10, 40]$  s in order to increase the signal-to-background ratio after applying the same muon track cut. A 10 s veto after each muon rejects the shorter-lived cosmogenic radionuclides, which decreases the live time of the data set by 28.4% and leaves  $^{11}\text{Be}$  as the only cosmogenic isotope. The background spectral shape is derived from events which satisfy the muon track cut and occur later than 210 s after the muon. The best fit results are shown in figure 9. The selection efficiency of the muon track cut is estimated to  $(63.3 \pm 2.5)\%$  using the time and lateral distribution of cosmogenic  $^{12}\text{B}$  to preceding muon

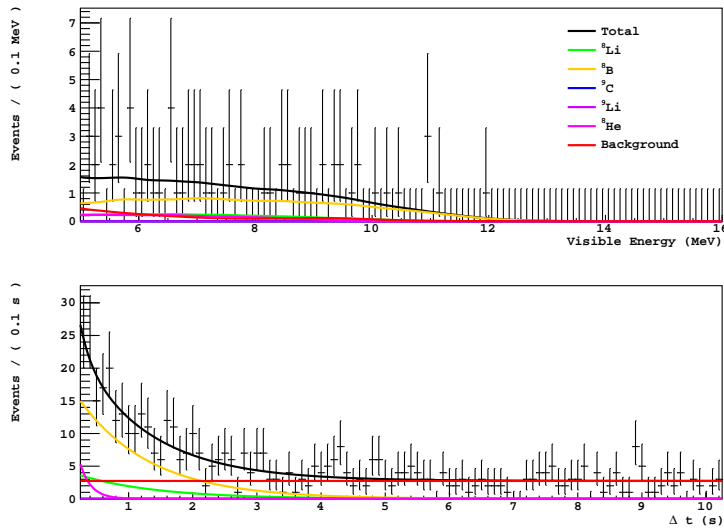


**Figure 8.** Simultaneous fit of the cosmogenic isotope  ${}^9\text{C}$  in visible energy deposition (top panel) and decay time relative to preceding muons (bottom panel). The fit returns only an upper limit for the isotope  ${}^9\text{C}$  and some isotopes which cannot be seen in the graph. The goodness of the simultaneous fit is  $\chi^2/\text{ndf} = 218/268$ .

tracks. The fraction of decays in the selected visible energy range is calculated to be  $\varepsilon({}^{11}\text{Be}) = (69.3 \pm 0.6)\%$ . The isotopic production rate and yield of  ${}^{11}\text{Be}$  are measured to be  $R({}^{11}\text{Be}) < 0.20 (\text{d } 100\text{t})^{-1}$  and  $Y({}^{11}\text{Be}) < 7.0 \cdot 10^{-7} / (\mu \cdot (\text{g}/\text{cm}^2))$  at the  $3\sigma$  confidence level.

## 5.6 ${}^{10}\text{C}$

The production of  ${}^{10}\text{C}$  ( $\beta^+$ -emitter,  $\tau = 27.8\text{ s}$ ,  $Q = 3.65\text{ MeV}$ ) in muon-induced spallation processes on  ${}^{12}\text{C}$  is usually accompanied by the emission of at least one free neutron. These neutrons are eventually captured on hydrogen or carbon (section 5.2). The accidental background is significantly reduced after requiring a three-fold coincidence between a muon, at least one subsequent neutron capture, and a  ${}^{10}\text{C}$  decay candidate. Neutron captures with a minimum energy of 1.3 MeV are selected inside the full neutron trigger gate of  $[16, 1600]\ \mu\text{s}$  after the muon event. Also  ${}^{10}\text{C}$  candidates must satisfy a cut in visible energy of  $[2, 4]\text{ MeV}$  and occur within  $[10, 310]\text{ s}$  to a preceding  $\mu n$ -coincidence. A lower energy threshold of 2 MeV avoids a contribution of  ${}^{11}\text{C}$  decays in the data set. The energy distribution of the  ${}^{10}\text{C}$  candidates is constructed from events with  $\Delta t \in [10, 50]\text{ s}$ . Only  ${}^{11}\text{Be}$  contributes as a cosmogenic contaminant in this parameter selection. Based on the selection cuts and the additional requirement of a  $\mu n$ -coincidence, the contribution of  ${}^{11}\text{Be}$  is estimated to be less than  $6 \cdot 10^{-3} (\text{d } 100\text{t})^{-1}$  and this is taken into account as a systematic uncertainty. The spectral shape of uncorrelated background is derived from events at  $\Delta t > 310\text{ s}$ . The simultaneous fit is depicted in figure 10. The fraction of  ${}^{10}\text{C}$  decays accompanied by a muon in coincidence with at least one detected neutron capture is estimated via a test sample of  ${}^{10}\text{C}$  candidates.  ${}^{10}\text{C}$  candidates are selected by  $\Delta t \in [10, 310]\text{ s}$  and a lateral distance of 1 m to a parent muon after removal of the neutron requirement. The numbers of  ${}^{10}\text{C}$  decays in the subset which satisfy the neutron requirements (subset A), as well as in the complementary subset (subset B), are derived by time profile fits and



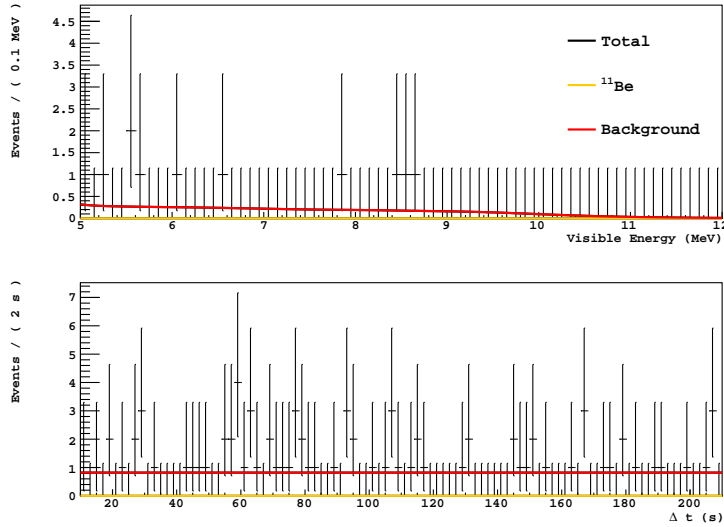


**Figure 9.** Simultaneous fit of the cosmogenic isotope  $^{11}\text{Be}$  in visible energy deposition (top panel) and decay time relative to preceding muons (bottom panel). The fit returns only an upper limit for the isotope  $^{11}\text{Be}$ . The goodness of the simultaneous fit is  $\chi^2/\text{ndf} = 30/61$ . We note, that the low value of the reduced  $\chi^2$  is connected to the low statistics of the data set fit in the unbinned maximum likelihood fit.

then compared. The  $^{10}\text{C}$  tagging efficiency due to the neutron requirement is evaluated to  $\varepsilon_n(^{10}\text{C}) = (92.5^{+7.5}_{-20.0})\%$ . The broad uncertainty range is associated with the determination of  $^{10}\text{C}$  decays in subset B, which is dominated by physically uncorrelated matches. Based on the Monte Carlo simulation, we expect  $\varepsilon(^{10}\text{C}) = (79.0 \pm 0.5)\%$  of all  $^{10}\text{C}$  decays within the selected energy range. By considering these corrections, the  $^{10}\text{C}$  rate and yield are determined by the simultaneous fit to  $R(^{10}\text{C}) = (0.52 \pm 0.07_{\text{stat}}^{+0.11}_{-0.06\text{sys}}) (\text{d } 100\text{t})^{-1}$  and  $Y(^{10}\text{C}) = (1.79 \pm 0.25_{\text{stat}}^{+0.38}_{-0.20\text{sys}}) \cdot 10^{-6} / (\mu \cdot (\text{g}/\text{cm}^2))$ .

## 5.7 $^{11}\text{C}$

Like  $^{10}\text{C}$ , neutron emission is expected in the muon-induced production of cosmogenic  $^{11}\text{C}$  which is a  $\beta^+$ -emitter, with  $\tau = 29.4 \text{ min}$ ,  $Q = 1.98 \text{ MeV}$ . Therefore, an analogous three-fold coincidence between a muon, subsequent neutron capture(s), and  $^{11}\text{C}$  candidates is applied in the rate determination. Candidates of  $^{11}\text{C}$  decays are selected within the energy range of  $[1, 2] \text{ MeV}$  and the time gate of  $[0.1, 3.6] \text{ h}$  with respect to a preceding muon-neutron coincidence. The events for the energy distribution are selected in the same time interval. As a result of the long lifetime of  $^{11}\text{C}$  and an average run duration of  $\sim 6 \text{ h}$  in Borexino, effects of run boundaries on the time profile are not negligible. To avoid a distortion of the time profile,  $^{11}\text{C}$  decays within the first 3.6 h after run start are not considered in the analysis. This restriction reduces the data set to a live time of 188 d. Events within 2 h and 4 m with respect to any neutron capture vertex of a  $\mu n$ -coincidence are vetoed to obtain the formation of the background spectral shape. The remaining events are used to derive a spectrum containing only  $\mu n$ -uncorrelated background sources, i.e. non-cosmogenic background, and  $^{11}\text{C}$  production without the detection of a subsequent neutron capture. The latter contribution is the result of the limited neutron detection efficiency, in case of saturated detector electron-

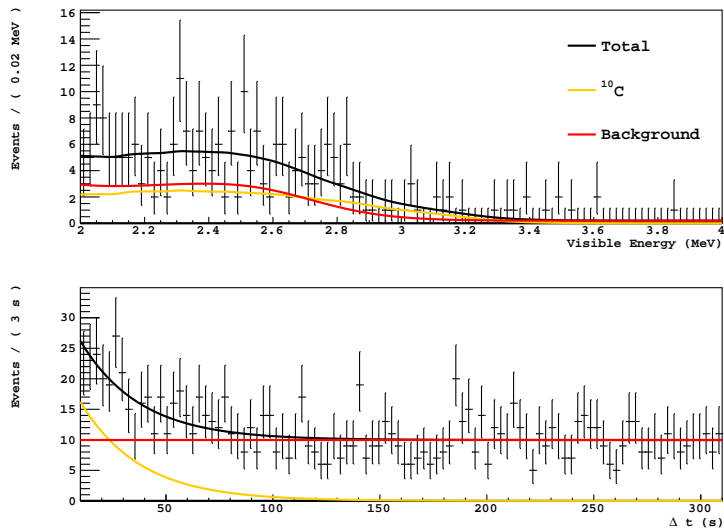


**Figure 10.** The simultaneous fit of the cosmogenic isotope  $^{10}\text{C}$  in visible energy deposition (top panel) and decay time relative to preceding muons (bottom panel). The goodness of the simultaneous fit is  $\chi^2/\text{ndf} = 153/162$ .

ics and so-called *invisible* channels. Invisible channels denote all muon-induced production processes, yielding  $^{11}\text{C}$  with no free neutron emission in the final state [9, 16].

The result of a simultaneous fit in energy and time is shown in figure 11. The fraction of  $^{11}\text{C}$  decays correlated with a muon and at least one detected neutron is estimated in the same manner as in the  $^{10}\text{C}$  analysis described in section 5.6. The selection of the subset of  $^{11}\text{C}$  candidates is chosen within  $\Delta t \in [0.1, 3.6]$  h and a lateral distance of 1 m to a preceding  $\mu n$ -coincidence. The obtained efficiency for the neutron requirement is  $\varepsilon_n(^{11}\text{C}) = (86.8 \pm 6.9)\%$ . The cosmogenic production rate is found to be  $R(^{11}\text{C}) = (25.8 \pm 1.3_{\text{stat}} \pm 3.2_{\text{syst}}) (\text{d } 100\text{t})^{-1}$  with a corresponding yield of  $Y(^{11}\text{C}) = (8.86 \pm 0.45_{\text{stat}} \pm 1.10_{\text{syst}}) \cdot 10^{-5} / (\mu \cdot (\text{g}/\text{cm}^2))$  after correcting for the fraction of  $\varepsilon(^{11}\text{C}) = (92.2 \pm 0.4)\%$  of all decays which deposit a visible energy in the selected parameter space. The rate of  $^{11}\text{C}$  decays detected in coincidence with cosmic muons and associated neutrons is in good agreement with results obtained from spectral fits without the coincidence requirement. Modeling all signal components in the energy range of [270, 1600] keV, the  $^{11}\text{C}$  rate was found to be  $R(^{11}\text{C}) = (28.5 \pm 0.2_{\text{stat}} \pm 0.7_{\text{syst}}) (\text{d } 100\text{t})^{-1}$  in the precision measurement of the solar  $^7\text{Be}$  neutrino interaction rate in Borexino [2].

## 6 Monte Carlo simulations of Cosmogenic Neutrons and Radioisotopes

The production of cosmogenic neutrons and radioisotopes in Borexino was studied by using the GEANT4 [17, 18] and FLUKA [19, 20] simulation packages which are both commonly used to simulate deep underground, low background experiments. Their predictions are compared with our experimental data.

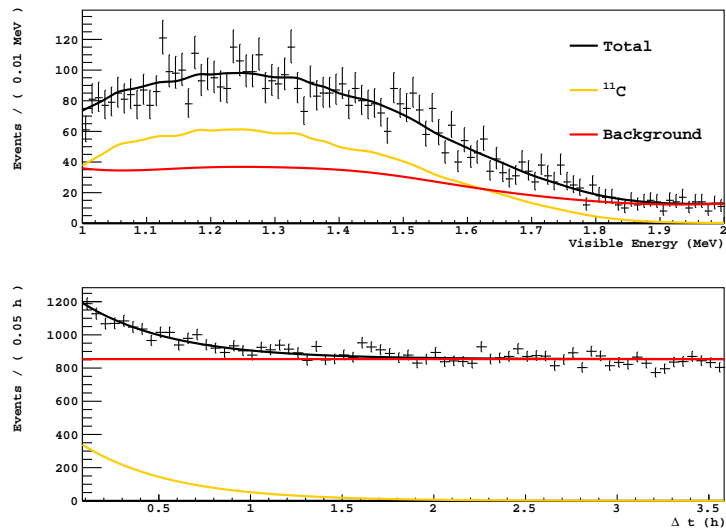


**Figure 11.** Simultaneous fit of the cosmogenic isotope  $^{11}\text{C}$  in visible energy deposition (top panel) and decay time relative to preceding muons (bottom panel). The goodness of the simultaneous fit is  $\chi^2/\text{ndf} = 189/168$ .

## 6.1 Simulation procedure

Initially, a careful description of the muon-induced radiation field at LNGS was prepared using FLUKA. For this simulation a model of Hall C is surrounded by a 700 cm thick shell of Gran Sasso rock [21] which is found sufficient to allow a full shower development. The setup is subjected to residual cosmogenic muons taking into account the muon angular distribution and the muon differential energy spectrum as a function of the slant depth and muon event multiplicity as measured by the MACRO experiment [12, 22]. The adopted muon charge ratio is  $R_\mu = N_{\mu^+}/N_{\mu^-} \simeq 1.38$  as measured by the OPERA experiment [23]. Cosmogenic muons and muon-induced secondaries emerging into Hall C are followed, and all particles reaching the Borexino water tank are recorded. Details of this simulation are given in [24].

A fraction of 1.5% of the cosmogenic events with multiple muons crossing the Borexino detector simultaneously is found from simulation. Further, 12% of single muon events are actually caused by single muons which belong to muon bundles.

The cosmogenic events which were recorded at the outside of the water tank are then used as a source for both GEANT4 and FLUKA to simulate the production of cosmogenic neutrons and radioisotopes inside the Borexino detector setup. The yields are extracted directly by recording neutron captures and residual isotope production, rather than simulating the full detector response. The Monte Carlo simulation predictions are compared to the data analysis results of the previous sections that include corrections for detection efficiency.

For the comparison between predictions and experimental data, the following observables are considered: 1) the rates for neutron captures and cosmogenic isotopes production, 2) the neutron capture time, 3) the neutron capture multiplicity for individual muon events, and 4) the lateral distance between the neutron capture and the parent muon track. We also compare the rate of muon events for which one or more neutron captures are recorded.

<b>Model I</b>	<b>HP</b>	<b>Binary</b>	<b>Bertini</b>	<b>FTF</b>
Protons		0 → 5 GeV		4 GeV → 100 TeV
Neutrons	0 → 20 MeV	19.9 MeV → 5 GeV		4 GeV → 100 TeV
$\pi$		0 → 5 GeV		4 GeV → 100 TeV
K			0 → 5 GeV	4 GeV → 100 TeV
<b>Model II</b>	<b>HP</b>	<b>Bertini</b>	<b>FTF</b>	
Protons		0 → 5 GeV	4 GeV → 100 TeV	
Neutrons	0 → 20 MeV	19.9 MeV → 5 GeV	4 GeV → 100 TeV	
$\pi$ , K		0 → 5 GeV	4 GeV → 100 TeV	
<b>Model III</b>	<b>HP</b>	<b>Binary</b>	<b>LEP</b>	<b>QGS</b>
Protons		0 → 9.9 GeV	9.5 → 25 GeV	12 GeV → 100 TeV
Neutrons	0 → 20 MeV	19.9 MeV → 9.9 GeV	9.5 → 25 GeV	12 GeV → 100 TeV
$\pi$ , K		0 → 9.9 GeV	9.5 → 25 GeV	12 GeV → 100 TeV
<b>Model IV</b>	<b>HP</b>	<b>Bertini</b>	<b>LEP</b>	<b>QGS</b>
Protons		0 → 9.9 GeV	9.5 → 25 GeV	12 GeV → 100 TeV
Neutrons	0 → 20 MeV	19.9 MeV → 9.9 GeV	9.5 → 25 GeV	12 GeV → 100 TeV
$\pi$ , K		0 → 9.9 GeV	9.5 → 25 GeV	12 GeV → 100 TeV

**Table 3.** Summary of the Hadronic Models used in GEANT4.

### 6.1.1 GEANT4

The version of GEANT4 which is used for this study is Geant4-09-06-patch-01 from February 2013. Detailed description of the GEANT4 toolkit is available in [25].

Many hadronic models are available in GEANT4 [26], and can be used as functions of the particle energy. We cover the entire muon energy spectrum at LNGS through a combination of different physics inputs. For our study, we use: a) the Quark-Gluon String (QGS) model for proton, neutron, pion and kaon interactions with nuclei at kinetic energies above 12 GeV, completed with the *Precompound* model for the evaporation phase of the interaction; b) the Fritiof model (FTF) for the interaction of highly energetic protons, neutrons, pions and kaons starting from 4-5 GeV, also completed with the *Precompound* model; c) the Bertini cascade (BERT) model, which includes intra-nuclear cascade, followed by precompound and evaporation phases of the residual nucleus, for proton, neutron, pion and kaon interactions with nuclei at kinetic energies below 9.9 GeV; d) the Binary cascade (BIC) model, a data driven intra-nuclear cascade model intended for energies below 5 GeV; e) the High Precision Neutron (HP) model, describing parameterized capture and fission for low-energy neutrons (below 20 MeV); f) the Low Energy Parameterized (LEP) model for proton, neutron, pion and kaon interactions with nuclei at kinetic energies between 9.5 GeV and 25 GeV.

Some “ready-made” Physics Lists merging different models are available, and we have defined four models: Model I (merge of FTF and BIC with HP manually added), Model II (merge of FTF, BERT and HP), Model III (merge of QGS, BIC and HP), Model IV (merge of QGS, BERT and HP). A summary of the introduced hadronic models is shown in table 3.

For each model, G4MuonNuclearProcess was used to simulate the muon-nuclear interactions. Below 10 GeV, the virtual photon is converted into a real photon and then interacts with the nucleus using the BERT model. Above 10 GeV, the virtual photon is converted into a  $\pi^0$  and the interaction with the nucleus is described by the FTF model [26].

Each model has been tested with and without the activation of the Light Ion (LI) Physics List (which defines the light ions likely to be produced by the hadronic interactions, such as deuterons, tritons,  $^3\text{He}$ ,  $\alpha$ -particles and generic ions). In addition, the following Physics Lists are included for each model: the Electromagnetic Processes for Lep-

tons (G4eMultipleScattering, G4eIonisation, G4eBremsstrahlung, ...), the Nuclear Decay Processes (G4Decay, G4RadioactiveDecay) and the standard Elastic Scattering for hadrons (G4HadronElasticPhysics).

### 6.1.2 FLUKA

FLUKA is a fully integrated particle physics Monte Carlo simulation package based predominantly on original and well-tested microscopic models. The models are benchmarked and optimized by comparing to experimental data at the single interaction level. The physics models in FLUKA are fully integrated into the code and no modifications or adjustments are available at the user level. A list of benchmark results relevant to the simulation of deep underground cosmogenic backgrounds is described in [24].

Details of the physics models implemented in FLUKA with focus on hadronic interactions and the FLUKA specific nuclear interaction model PEANUT can be found in [27–30], while a description of the approach for muon interactions in FLUKA is given in [31]. A validation of the FLUKA Monte Carlo code for predicting induced radioactivity is given, for instance, in [32].

In general, the simulation was performed using the FLUKA default setting PRECISIO(n). In addition, photonuclear interactions were enabled through the FLUKA option PHOTONUC and a more detailed treatment of nuclear de-excitation was requested with the EVAPORAT(ion) and COALESCE(nce) options. These enable the evaporation of heavy fragments ( $A > 1$ ) and the emission of energetic light fragments, respectively. The treatment of nucleus-nucleus interaction was turned on for all energies via the option IONTRANS and radioactive decays were activated through the option RADDECAY.

The version of FLUKA used for the present study is FLUKA2011.2, released in November 2011. Further information about the implemented physics models is available through the FLUKA manual and additional documentation and lecture notes located at the official FLUKA website [33].

## 6.2 Simulation results

We present the predictions obtained with GEANT4 and FLUKA regarding different physics observables. For GEANT4, we concluded that the best match to data is given by Model III or IV, depending on the observable under study. Model I produced 15% less neutrons than the other models and Model II shows no relevant difference with respect to model IV. For readability we choose to present here only Model III and IV, however complete results for all four models are available as supplementary material of this article.

### 6.2.1 Cosmogenic Radioisotopes

Production yields for cosmogenic isotopes and neutrons are summarized in table 4. The yields measured by Borexino are compared to GEANT4 and FLUKA predictions as well as measured yields from the KamLAND experiment [9] given in the rightmost column. We note that KamLAND has a different number of carbon nuclei per ton of liquid scintillator ( $4.30 \cdot 10^{28}$  for KamLAND as opposed to  $4.52 \cdot 10^{28}$  in case of Borexino) and that the mean residual muon energies differ somewhat between the two sites:  $(283 \pm 19)$  GeV at LNGS<sup>2</sup> versus  $(260 \pm 8)$  GeV at the Kamioka mine [9], which should lead to a difference in the observed production yields.

<sup>2</sup> The residual mean muon energy is based on the MACRO measurement for single and double muon events reported in [34]. Details of the procedure are given in [24].

	GEANT4 Model III	GEANT4 Model IV	FLUKA	Borexino	KamLAND
	— $\langle E_\mu \rangle = 283 \pm 19 \text{ GeV}$ —			$\langle E_\mu \rangle = 260 \pm 8 \text{ GeV}$	
Isotopes	Yield $[10^{-7} (\mu \text{ g/cm}^2)^{-1}]$				
$^{12}\text{N}$	$1.11 \pm 0.13$	$3.0 \pm 0.2$	$0.5 \pm 0.2$	$< 1.1$	$1.8 \pm 0.4$
$^{12}\text{B}$	$30.1 \pm 0.7$	$29.7 \pm 0.7$	$28.8 \pm 1.9$	$56 \pm 3$	$42.9 \pm 3.3$
$^8\text{He}$	$< 0.04$	$0.18 \pm 0.05$	$0.30 \pm 0.15$	$< 1.5$	$0.7 \pm 0.4$
$^9\text{Li}$	$0.6 \pm 0.1$	$1.68 \pm 0.16$	$3.1 \pm 0.4$	$2.9 \pm 0.3$	$2.2 \pm 0.2$
$^8\text{B}$	$0.52 \pm 0.09$	$1.44 \pm 0.15$	$6.6 \pm 0.6$	$14 \pm 6$	$8.4 \pm 2.4$
$^6\text{He}$	$18.5 \pm 0.5$	$8.9 \pm 0.4$	$17.3 \pm 1.1$	$38 \pm 15$	not reported
$^8\text{Li}$	$27.7 \pm 0.7$	$7.8 \pm 0.4$	$28.8 \pm 1.0$	$7 \pm 7$	$12.2 \pm 2.6$
$^9\text{C}$	$0.16 \pm 0.05$	$0.99 \pm 0.13$	$0.91 \pm 0.10$	$< 16$	$3.0 \pm 1.2$
$^{11}\text{Be}$	$0.24 \pm 0.06$	$0.45 \pm 0.09$	$0.59 \pm 0.12$	$< 7.0$	$1.1 \pm 0.2$
$^{10}\text{C}$	$15.0 \pm 0.5$	$41.1 \pm 0.8$	$14.1 \pm 0.7$	$18 \pm 5$	$16.5 \pm 1.9$
$^{11}\text{C}$	$315 \pm 2$	$415 \pm 3$	$467 \pm 23$	$886 \pm 115$	$866 \pm 153$
Neutrons	Yield $[10^{-4} (\mu \text{ g/cm}^2)^{-1}]$				
	$3.01 \pm 0.05$	$2.99 \pm 0.03$	$2.46 \pm 0.12$	$3.10 \pm 0.11$	$2.79 \pm 0.31$

**Table 4.** Predicted yields for cosmogenic products obtained from GEANT4 (Model III and IV) and FLUKA are compared to data from Borexino . Also shown are results from the KamLAND experiment [9]. Note that the production yields depend on the number of carbon atoms per weight and the muon energy spectrum. Thus, a 10–20% difference between KamLAND and Borexino results is expected.

### 6.2.2 Cosmogenic neutrons

**Neutron capture time.** The simulated neutron capture time of the Borexino scintillator from GEANT4 and FLUKA are  $(275.8 \pm 0.9) \mu\text{s}^3$  and  $(253.4 \pm 0.6) \mu\text{s}$ , respectively. This is to be compared to the measured capture time of  $(259.7 \pm 1.3_{\text{stat}} \pm 2.0_{\text{syst}}) \mu\text{s}$ . The neutron capture time was also measured in Borexino using an Am-Be neutron source [11] which yields  $(254.5 \pm 1.8) \mu\text{s}$ . The experimental disagreement with the value measured from cosmogenic neutrons could be explained by a fraction of neutrons which are captured on iron in the source capsule. This was also observed by KamLAND [9].

**Neutron production yield.** In table 4, the neutron production yield is reported. The observed neutron production deficit of the FLUKA simulation was studied in [24]. The main cause of the deficit was found to be the low cosmogenic production rate predicted for  $^{11}\text{C}$  (table 4). At the LNGS depth, the production of  $^{11}\text{C}$  in liquid scintillator is followed by a neutron emission in 95% of all cases as was shown by [16]. Since the measured  $^{11}\text{C}$  rate is almost 30% of the neutron production rate, and the  $^{11}\text{C}$  rate given by FLUKA is roughly 50% of the measured value, a reduction of the number of predicted cosmogenic neutrons in the order of 15% is expected. The origin of the low  $^{11}\text{C}$  production rate in FLUKA is addressed by improvements to the Fermi break-up model [35, 36] which will be available with the next FLUKA release. The impact of the improved model for the  $^{11}\text{C}$  production in liquid scintillator at LNGS energies is currently under investigation. In addition, FLUKA predicts the production of energetic deuterons ( $E_{\text{kin}} > 50 \text{ MeV}$ ) inside the liquid scintillator

<sup>3</sup>The out-dated GEANT4 version 4.9.2.p02 returns  $(254.9 \pm 0.6) \mu\text{s}$  and is thus in agreement with the measured value. No explanation has been found for the discrepancy between the different GEANT4 versions.

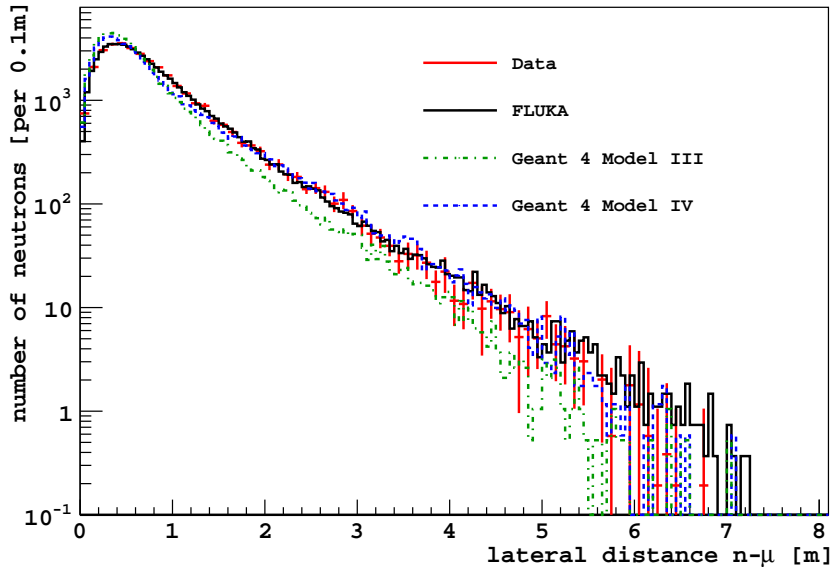


**Figure 12.** Lateral distance between neutron capture points and the parent muon track: comparison of Borexino data to predictions obtained with GEANT4 - Model III and IV and FLUKA .

with a rate approximately equal to 4% of the cosmogenic neutron production rate. Energetic deuterons can re-interact with the scintillator leading to a break up (and re-capture) of the neutrons. However, these processes are not described by FLUKA as no interaction model is yet implemented for these deuterons. This further reduces the predicted number of cosmogenic neutrons.

The neutron yield of the GEANT4 simulation is in good agreement with the data, but the  $^{11}\text{C}$  rate is also  $\sim 50\%$  of the measured value. As  $^{11}\text{C}$  is usually produced together with a neutron, this indicates that the yields of other neutron production channels are too high in GEANT4.

The neutron production yield measured by the KamLAND experiment is  $(2.79 \pm 0.31) \cdot 10^{-4} \text{ n}/\mu \cdot (\text{g}/\text{cm}^2)$  [9]. The latest results from the LVD experiment, which is also located at LNGS, indicate a neutron yield of  $(2.9 \pm 0.6) \cdot 10^{-4} \text{ n}/\mu \cdot (\text{g}/\text{cm}^2)$  [37].

**Muon-neutron lateral distance distribution.** The lateral distance distribution of the neutron capture location from the parent muon track is shown in figure 12 and compared to predictions from simulation. As described in section 4.4, a radial cut of less than 4 m for neutrons and an impact parameter cut less than 4 m for muons were applied in the simulations. Moreover, the muon track reconstruction uncertainties were applied *a posteriori* to the simulated distribution. They dominate the shape at small distances. The simulated distributions were scaled to match the number of measured neutron captures in order to compare the shape of the histograms. The experimental distribution is well reproduced by both GEANT4 - Model IV and FLUKA out to large distances. GEANT4 - Model III instead reproduces data less accurately. The small differences present at the far range can be attributed to the additional cuts described in section 4.4, which have not been implemented in the simulation. They mostly suppress mis-reconstructed neutrons following showering muons which are expected to dominate the distribution at large distances from the track.

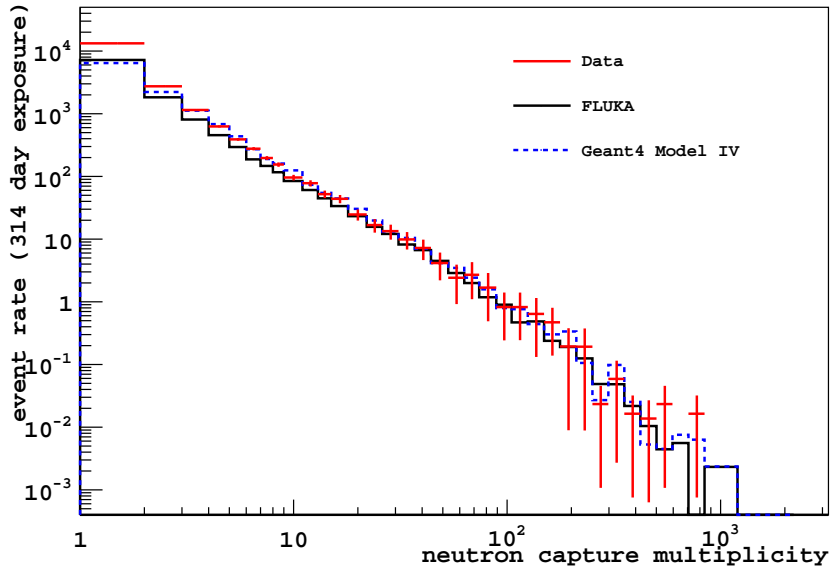


**Figure 13.** Neutron capture multiplicity: comparison of Borexino data to predictions obtained with GEANT4 - Model IV and FLUKA . Simulated curves were modified to account for the limited neutron detection window  $[30 - 1590] \mu\text{s}$  after the muon. GEANT4 - Model III curve does not differ appreciably from Model IV curve and is not shown.

**Neutron capture multiplicity.** The neutron capture multiplicity distribution is shown in figure 13, for the the experimental spectrum as obtained from SYS1 (section 4.2). The experimental distribution is compared to predictions by GEANT4 - Model IV and FLUKA which were both scaled to match the live time of the experimental data set. With the exception of events with low multiplicities, good overall agreement between data and simulation is found for both packages out to multiplicities of hundreds of neutron captures. The shape of the multiplicity distribution is somewhat distorted towards small multiplicities for both Monte Carlo simulations and data with respect to the true physical distribution, because neutrons are only detected if they are captured between 30 and 1590  $\mu\text{s}$  after the muon trigger.

**Rate of neutron-producing muons.** The rate of cosmic muons crossing Borexino which produce at least one neutron is not well reproduced by both simulation packages. The measured rate is  $67 \pm 1$  events per day, while FLUKA returns  $41 \pm 3$  per day and GEANT4 returns  $42.5 \pm 0.2$  (Model III) and  $44.6 \pm 0.2$  (Model IV). This discrepancy is also apparent from the multiplicity plot in figure 13 and seems to be associated with low multiplicity events. No explanation has been found for this discrepancy.

## 7 Conclusions

The Borexino detector offers a unique opportunity to study cosmic backgrounds at a depth of 3800 m w.e. at the Gran Sasso underground laboratories. The results are not only essential to low-energy neutrino analyses, but are also of substantial interest for direct dark matter and  $0\nu\beta\beta$  searches at underground facilities. Based on thermal neutron captures in the scintillator target of Borexino, a spallation neutron yield of  $Y_n = (3.10 \pm 0.11) \cdot 10^{-4} n / (\mu \cdot (\text{g}/\text{cm}^2))$  was



determined. The lateral distance profile was measured based on the reconstructed parent muon tracks and neutron capture vertices. An average lateral distance of  $\lambda = (81.5 \pm 2.7)$  cm was found. The data results on neutron yield, multiplicity and lateral distributions were compared to Monte Carlo simulation predictions by the FLUKA and GEANT4 framework and are largely compatible. The simulated neutron yield of FLUKA shows a deficit of  $\sim 20\%$ , while the result of the GEANT4 simulation is in good agreement with the measured value. However, both simulations should be increased as a result on an underprediction of  $^{11}\text{C}$  production.

The production rates of several cosmogenic radioisotopes in the scintillator were determined based on a simultaneous fit to energy and decay time distributions. Results of a corresponding analysis performed by the KamLAND collaboration for the Kamioka underground laboratory [9] are similar to our findings. Moreover, Borexino rates were compared to predictions by FLUKA and GEANT4: While there is good agreement within their uncertainties for most isotopes, some cases ( $^{12}\text{B}$ ,  $^{11}\text{C}$ ,  $^8\text{Li}$  for both codes and  $^8\text{B}$ ,  $^9\text{Li}$  for GEANT4 only) show a significant deviation between data and Monte Carlo simulation predictions.

## Acknowledgements

The Borexino program is made possible by funding from INFN (Italy), NSF (USA), BMBF, DFG (OB 168/1-1), MPG, and the Garching accelerator laboratory MLL (Germany), Russian Foundation for Basic Research (Grant 12-02-12116) (Russia), MNiSW (Poland), and the UnivEarthS LabEx programme (ANR-11-IDEX-0005-02) (France). We acknowledge the generous support of the Gran Sasso National Laboratory (LNGS).

## References

- [1] Borexino coll., C. Arpesella *et al.*, Phys. Rev. Lett. **101**, 091302 (2008).
- [2] Borexino coll., G. Bellini *et al.*, Phys. Rev. Lett. **107**, 141302 (2011).
- [3] Borexino coll., G. Bellini *et al.*, Phys. Rev. **D82**, 033006 (2010).
- [4] Borexino coll., G. Bellini *et al.*, Phys. Rev. Lett. **108**, 051302 (2012).
- [5] Borexino coll., G. Bellini *et al.*, Phys. Lett. **B687**, 299 (2010).
- [6] Borexino coll., G. Bellini *et al.*, accept. for publ. on Phys. Lett. B (2013), arXiv:1303.2571.
- [7] L. Cadonati, F. Calaprice, and M. Chen, Astropart. Phys. **16**, 361 (2002).
- [8] B. Dasgupta and J. Beacom, Phys.Rev. **D83**, 113006 (2011).
- [9] KamLAND coll., S. Abe *et al.*, Phys. Rev. **C81**, 025807 (2010).
- [10] Borexino coll., G. Alimonti *et al.*, Nucl. Inst. and Meth. **A600**, 568 (2009).
- [11] Borexino coll., G. Bellini *et al.*, JINST **6**, P05005 (2011).
- [12] MACRO coll., M. Ambrosio *et al.*, Astropart. Phys. **19**, 313 (2003).
- [13] Borexino coll., G. Bellini *et al.*, JCAP **05**, P015 (2012).
- [14] International Atomic Energy Agency, <http://www.iaea.org>.
- [15] LVD coll., M. Aglietta *et al.*, In Proc. of 26<sup>th</sup> ICRC, Salt Lake City (USA) (1999).
- [16] C. Galbiati *et al.*, Phys. Rev. **C71**, 055805 (2005).
- [17] GEANT4 coll., Nucl. Instr. and Meth. A **506**, 250 (2003).
- [18] Geant4 coll., IEEE, Transactions on Nuclear Science **53**, 1, 270 (2006).

- [19] G. Battistoni *et al.*, AIP Conference Proceeding **896**, 31 (2007).
- [20] A. Ferrari, P. R. Sala, A. Fassò, and J. Ranft, CERN-2005-10 (2005), INFN/TC\_05/11, SLAC-R-773 (2005).
- [21] H. Wulandari *et al.*, Astropart. Phys. **22**, 313 (2004).
- [22] MACRO coll., J. T. Hong *et al.*, in Proc. 8<sup>th</sup> ISVHECRI, Tokyo (Japan) (1994).
- [23] OPERA coll., N. Agafonova *et al.*, Eur. Phys. J. **C 67**, 25 (2010).
- [24] A. Empl, R. Jasim, Ed Hungerford and P. Mosteiro, (2012), arXiv:1210.2708.
- [25] <http://www.geant4.org/geant4/results/publications.shtml>.
- [26] GEANT4, Physics reference manual, <http://geant4.web.cern.ch/geant4/UserDocumentation/UsersGuides/PhysicsReferenceManual/fo/PhysicsReferenceManual.pdf>.
- [27] A. Fassò and A. Ferrari and J. Ranft and P. R. Sala, Proceedings of the MonteCarlo 2000 Conference, Lisbon , 159 (2001).
- [28] A. Fassò and A. Ferrari and J. Ranft and P. R. Sala, Proceedings of the "Specialists' Meeting on Shielding Aspects of Accelerators, Targets & Irradiation Facilities, Arlington" (1995).
- [29] A. Ferrari and P. R. Sala, Proceedings of Workshop on Nuclear Reaction Data and Nuclear Reactors Physics, Design and Safety, Trieste (1998).
- [30] G. Battistoni and others, Proceedings of 11th International Conference on Nuclear Reaction Mechanism, Varenna (2006).
- [31] Y.-F. Wang *et al.*, Phys. Rev. D **64**, 013012 (2001).
- [32] M. Brugger, A. Ferrari, S. Roesler, and L. Ulrici, NIM in Physics Research **A562**, 814 (2006).
- [33] FLUKA official website, <http://www.fluka.org>.
- [34] M. Ambrosio, the MACRO Collaboration, Astropart. Phys. **19**, 313 (2003), arXiv:hep-ex/0207043v2.
- [35] F. Cerutti and A. Ferrari and A. Mariani and P.R. Sala, Proc. 13th International Conference on Nuclear Reaction Mechanisms, Varenna (2012).
- [36] T. T. Bolen and others, Proc. of International Conf. on Nuclear Data for Science and Technology, New York, in press (2013).
- [37] LVD Collaboration, R. Persiani, poster at the Workshop in Low Radioactivity Techniques LRT 2013, LNGS Assergi (AQ), Italy, April 10-12, (2013).